Dalton Transactions

Check for updates

Enhancement in the performance of $Nb_{14}W_3O_{44}$ high power anodes through P doping in the tetrahedral sites

A. J. Green, [ID] *[a,b] J. W. Annis, [ID] [a,b] D. J. Gardner, [a,b] A. Spiller, [a] P. K. Allan [ID] [a,b] and P. R. Slater [ID] *[a,b]

Niobium-based anodes are emerging as promising candidates for high-power lithium-ion batteries due to their high theoretical capacities, robust safety at high current densities, and excellent long-term cycling stability. In this respect $Nb_{14}W_3O_{44}$ (NWO) has been attracting significant interest, and in this work, we investigate for the first time phosphorous-doping into this phase. Structural characterisation confirmed the substitution of phosphorous into the tetrahedral sites of the NWO framework, with a resulting contraction in the unit cell dimensions. Electrochemical testing demonstrated superior capacities for the P-doped materials, attributed to the replacement of W in the tetrahedral sites by non-reducible P, with a corresponding increase in W content in the octahedral sites. The P doped samples also showed excellent rate capability, with $x = 0.5$ and $x = 1$ retaining high capacities of 180(5) and 190(10) mAh g^{-1} at 2 A g^{-1}, respectively and 163(15) and 166(12) mAh g^{-1} at 4 A g^{-1} respectively, which could be additionally related to the P doping reducing particle size, which shortens lithium-ion diffusion paths. These results suggest further studies are warranted on the effect of such site-selective doping on the structure and morphology control, and the resulting influence on the electrochemical properties, in other Wadsley Roth niobate anodes with tetrahedral sites.

Introduction

Research to meet Net Zero targets has intensified the focus on lithium-ion battery (LiB) technology, which is crucial for enabling technologies that aim to reduce emissions and transform energy infrastructures. LiBs are central to many modern advancements, powering a vast array of devices from smartphones to electric vehicles (EVs), and facilitating large-scale energy storage solutions. The development of LiBs is focused on enhancing capacity, power, cycle longevity, cost-efficiency, and safety. The performance of these batteries is determined by a number of factors such as capacity, operating voltage, Li-ion conductivity, and electron transport, making advancements in these areas essential for the widespread adoption and commercialisation of LiB technology.[1–3]

Graphite is the dominant anode material in LIBs due to its cost-effectiveness, durability, high energy density, and theoretical capacity (372 mAh g^{-1}).[4] However, safety concerns at high (dis)charge rates limit its use in high-power applications such

a School of Chemistry, University of Birmingham, Edgbaston, Birmingham, B15 2TT, UK. E-mail: p.r.slater@bham.ac.uk
b The Faraday Institution, Harwell Campus, Didcot, OX11 0RA, UK

as power tools, drones, battery-powered forklifts, mining trucks, maritime and rail transport.[5] $Li_4Ti_5O_{12}$ (175 mAh g^{-1}, LTO)[6] spinel is a suitable alternative to graphite, providing a fast-charging solution. This material boasts favourable attributes in terms of safety and rate capability, as its higher operating voltage (1.55 V *vs.* Li/Li$^+$) eliminates the risk of lithium dendrite formation.[7–9] However, despite these advantages, LTO results in a lower energy density for the overall battery compared to a graphite anode cell, due to its' lower capacity and higher operating voltage.[10,11]

In recent years, niobium oxide systems have emerged as promising anode materials for high-power applications due to their improved energy density and enhanced safety. Their high working potential prevents lithium plating, thus avoiding lithium dendrite formation, which guarantees better battery safety. Additionally, they benefit from multi-electron redox reactions (Nb^{5+}/Nb^{4+} and Nb^{4+}/Nb^{3+}) that enhance the materials energy density compared to LTO.[12–14] These niobium oxide systems have Wadsley–Roth type structures which consist of ReO_3 like networks (blocks of distorted MO_6 octahedra which share corners), with crystallographic shear planes (edge-sharing of octahedra) that allow the accommodation of oxygen off-stoichiometry. The ReO_3 units are arranged in ($n \times m$) arrays, indicating the number of MO_6 octahedra along the

blocks' length and width, respectively, with block size determined by the metal-to-oxygen ratio.[12] Adjacent blocks are connected through edge-sharing octahedra or a combination of edge-sharing octahedra along with tetrahedrally coordinated metal atoms at the block corners.[13,15,16] These crystallographic shear planes provide structural rigidity, restricting the degree of rotation of the MO_6 octahedra, and facilitating rapid lithium-ion diffusion. These characteristics reduce volumetric expansion upon cycling, thus limiting degradation of the system.

These niobate systems have been intensely studied in the literature with the most common compositions being TiO_2–Nb_2O_5,[14,17–22] and WO_3–Nb_2O_5.[23–28] A wide range of other Wadsley–Roth niobate phases have also been reported in the literature.[29–32] The WO_3–Nb_2O_5 phase diagram has been extensively studied in the literature with Griffith et al. highlighting the excellent electrochemical properties of $Nb_{16}W_5O_{55}$ and $Nb_{18}W_{16}O_{63}$.[33] Driscoll et al. synthesised $Nb_9Ti_{1.5}W_{1.5}O_{30}$ through a co-doping strategy which showed enhanced delithiation capacities at 2 A g^{-1} (184 mAh g^{-1}); this doping strategy allowed the W content to be drastically reduced,[34,35] which is significant given tungsten's high cost and conflict mineral status.

One of the most studied compositions in the WO_3–Nb_2O_5 phase diagram is $Nb_{14}W_3O_{44}$ (Fig. 1) (NWO) which was first reported by Roth and Wadsley in 1965.[36] NWO has a (4 × 4) block structure with the oxygen off-stoichiometry additionally balanced by tetrahedrally coordinated metal atoms at the block corners.[37]

It has been previously shown that redox-active cations occupying tetrahedral sites can negatively impact the performance of niobate systems, leading to significant first-cycle capacity loss due to the irreversible reduction associated with the subsequent displacement of cations from tetrahedral to octahedral sites. This phenomenon is particularly significant in the (3 × 3) block compositions with VNb_9O_{25} and $Nb_7Ti_{1.5}Mo_{1.5}O_{25}$ experiencing large first-cycle losses, while PNb_9O_{25} (non-redox active P in the tetrahedral site) shows minimal loss in the first few cycles.[30,39–41]

Given these past observations. Here we investigate the synthesis, structure and electrochemical insights into new P-doped NWO phases, with the aim to substitute P into the tetrahedral site. The results show successful synthesis with the P-doped materials showing enhanced electrochemical performance compared to NWO highlighting their potential use in high-power LIB applications.

Experimental

Sample preparation

$Nb_{14-x}P_xW_3O_{44}$ (x = 0, 0.5 and 1) samples were prepared using the standard solid-state method, where x = 1 would correspond to complete filling of the tetrahedral site by P. Stoichiometric amounts of Nb_2O_5, WO_3, and $NH_4H_2PO_4$ were weighed out and ground together in an agate pestle and mortar, before heating in an alumina crucible. NWO (x = 0) was initially heated at 850 °C for 12 hours at a ramp rate of 5 °C min^{-1} under air. The sample was reground and reheated for a further 12 hours at 1100 °C at a ramp rate of 5 °C min^{-1} under air. The x = 0.5 and x = 1 samples were initially heated at 650 °C for 12 hours at a ramp rate of 5 °C min^{-1} in a fume cupboard in air to decompose the $NH_4H_2PO_4$, and after intermittent grinding at room temperature, was re-heated up to 1100 °C for 12 hours at a ramp rate of 5 °C min^{-1} in air.

Powder X-ray diffraction

Phase purity was confirmed by powder X-ray diffraction (PXRD) using a Bruker D8 diffractometer between 15–60° 2θ (Cu K$_{\alpha1+2}$). For structure determination, data were collected between 15–60° 2θ on a PANalytical Empyrean diffractometer (Cu K$_{\alpha1+2}$) using a flat plate reflection setup, and for more accurate structure determination on a STOE STADI P diffractometer between 2–70° 2θ (Mo K$_{\alpha1}$) using a spinning capillary setup with a 0.5 mm borosilicate glass capillary. Rietveld refinements were conducted using GSAS II.[42]

Scanning electron microscopy (SEM)

Scanning electron microscopy (SEM) images were collected on a Hitachi TM4000 plus tabletop microscope using back scattering electrons at a magnification of ×1500 and 15 kV.

Raman spectroscopy

Raman spectra were obtained using a Renishaw inVia Raman microscope equipped with a 532 nm laser line set at 1% power. The exposure time for each measurement was 10 seconds, with data accumulated over five acquisitions, covering the spectral range from 50 to 1500 cm^{-1}.

Coating and cell fabrication

The electrode slurry was prepared using an 90 : 5 : 5 ratio of active material (AM), carbon black (CB), and polyvinylidene fluoride (PVDF) using a THINKY mixer. The binder – polyvinylidene difluoride (PVDF) – was mixed with N-methyl pyrrolidone (NMP) initially for 5 min/1500 rpm, before additions of the
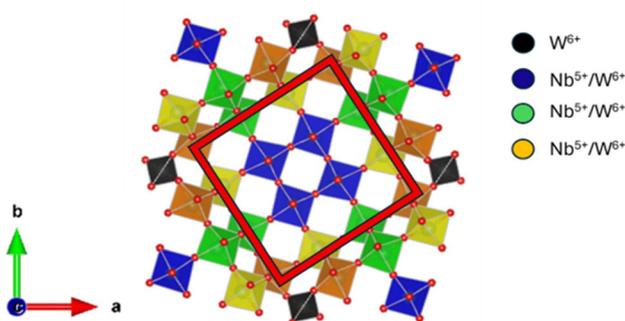

Fig. 1 Crystal structure of the NWO Wadsley–Roth material, drawn using the VESTA software.[38] The (4 × 4) block structure is highlighted by the red square. The tetrahedral sites (black tetrahedra), corner-sharing sites (blue octahedra), and edge-sharing sites (green and orange octahedra) in the structure are shown.

Legend: W^{6+} ; Nb^{5+}/W^{6+} ; Nb^{5+}/W^{6+} ; Nb^{5+}/W^{6+}

carbon black (C45) and the active material, with subsequent additions of NMP to produce a slurry (5 min/1500 rpm and 10 min/1500 rpm respectively). Copper foil was cut, placed on a vacuum platform, and smoothed using isopropyl alcohol (IPA) and a tissue. The slurry was poured onto the copper current collector, and the coating was applied using a doctor blade set to a height of 200 µm. The coating was initially dried at 80 °C for 45 minutes, then placed in a vacuum oven at 110 °C overnight for final drying. The coatings were then calendered using an MSK-HRP-01 hot rolling press at 80 °C until the porosity of the coated material was approximately between 30–40%.

The lithium-half cells were fabricated in an argon-filled glovebox. Initially, circular disks of the coated active material were cut to 12 mm in diameter and weighed outside the glovebox before being transferred inside. Steel 2032 cases were used. The lithium metal electrode was prepared from a dispensed fraction of lithium ribbon, with the surface scratched using a stainless-steel spatula to remove the tarnished surface and create a shiny, rough texture, then cut to a size of 12.7 mm for assembly. The electrolyte used was 1.0 M $LiPF_6$ in a 50 : 50 (v/v) mixture of ethylene carbonate and dimethyl carbonate, with two 50 µL additions made during assembly. A glass fibre separator was cut to 14.3 mm. Construction of the coin cells was conducted under an argon atmosphere. The lithium metal was placed on the cell lid, followed by the addition of 50 µL of $LiPF_6$ electrolyte. The glass microfiber separator was then positioned on top and coated with an additional 50 µL of $LiPF_6$ electrolyte. The anode material, spacer, and spring were sequentially added, and the assembly was finalised by crimping the cell lid. All cells had an active mass loading of between 3.00–3.12 mg cm^{-2}.

Electrochemical testing

The electrochemical performances of the materials were evaluated using a BioLogic BCS805 battery tester, with the cells cycled between 1.0–2.5 V in galvanostatic mode. All cells underwent formation cycling at a current density of 0.01 A g^{-1} within the specified voltage limits. During lithiation, a constant voltage step was applied at the lower voltage limit (1 V), which was maintained for 3 hours or until the current rate decayed to 20% of the initial value. Additionally, a 15 minutes rest period was incorporated between each cycle.

The rate studies for these materials were performed asymmetrically. During lithiation, a consistent current density of 0.1 A g^{-1} was applied with a constant voltage step until the current decayed to 20% of the initial value. The delithiation rate was progressively increased from 0.1 to 4 A g^{-1}, with 5 cycles at each step. Asymmetric cycling was employed to mitigate current rate limitations associated with using lithium metal in an organic electrolyte.[31] Following the rate study, an additional five cycles were conducted at 0.1 A g^{-1}, to assess degradation. For each measurement, two cells were tested under identical conditions to determine the average (de)lithiation capacities and the associated standard deviation, which is indicated in parentheses in the text.

Longer-term cycling was performed using a BioLogic BCS805 battery tester, with the cell being cycled between 1.0–2.5 V in galvanostatic mode. 100 cycles at 0.6 A g^{-1} were performed for each cell.

Results and discussion

Characterisation

The crystal structure and phase purity of the $Nb_{14-x}P_xW_3O_{44}$ (x = 0, 0.5 and 1) samples were investigated using PXRD (Fig. 2). The diffraction patterns show that both P-doped samples exhibit similar patterns to the undoped sample, with small shifts to higher 2θ values as the amount of P increased from x = 0 to x = 1, consistent with a reduction in lattice parameters associated with the substitution of Nb^{5+} by the smaller P^{5+}. The x = 0 and 0.5 samples showed no evidence of any impurity phases, with the XRD peaks matching the characteristic reflections of the tetragonal NWO structure (space group $I4/m$), indicating successful substitution of phosphorous into the lattice. The x = 1 sample showed slight shoulders and small extra peaks, as shown in Fig. S2, indicating a small amount of secondary phases, and suggesting that the P incorporation limit had been reached.

To further validate successful phosphorous doping, Rietveld refinements were performed to determine the cell parameters for the $Nb_{14-x}P_xW_3O_{44}$ (x = 0, 0.5 and 1) samples. In the case of the undoped (x = 0) and x = 0.5 samples, a good quality fit to the data was obtained, with corresponding refinement patterns shown in the Fig. S1a and b. As noted above, the x = 1 sample contained small extra peaks attributed to a small amount of a secondary phase (Fig. S1c). As summarised in Table 1, increasing phosphorous content leads to a systematic decrease in lattice parameters and unit cell volume, confirming the expected lattice contraction due to phosphorous incorporation (Fig. S3).

To enhance the reliability of the structural analysis, additional refinements were performed using a spinning capillary setup. This approach effectively suppressed contributions from preferred orientation, thereby improving the quality of
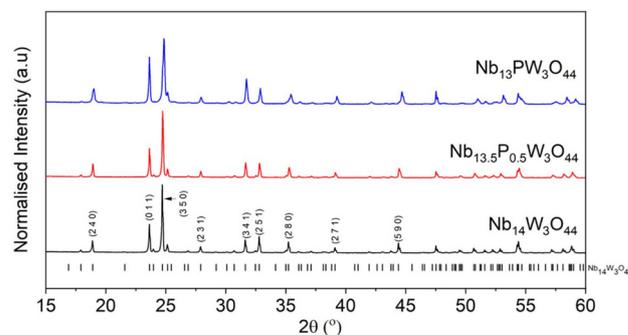

Fig. 2 PXRD patterns of $Nb_{14}W_3O_{44}$ (black), $Nb_{13.5}P_{0.5}W_3O_{44}$ (red) and $Nb_{13}PW_3O_{44}$ (blue), Cu Kα, with the lattice planes shown in brackets for specific peaks. Tick marks for $Nb_{14}W_3O_{44}$ are shown (black ticks).

Table 1 Unit cell parameters (tetragonal unit cell) of $Nb_{14-x}P_xW_3O_{44}$ (x = 0, 0.5, 1)

x	$a = b$ (Å)	c (Å)	Volume (Å^3)
0	20.9889(3)	3.82316(4)	1684.23(4)
0.5	20.9575(3)	3.82083(4)	1678.18(5)
1	20.8566(6)	3.81916(5)	1661.32(5)

the fits and yielding more reliable structural parameters. The corresponding refinement plots are provided in Fig. S4, with the structural parameters for all three phases tabulated in Tables S1–S3.

The morphology of the three samples was examined using SEM. The undoped (x = 0) sample (Fig. 3a) displays a heterogeneous mixture of thick and thin rod-like particles. Upon partial phosphorous substitution (x = 0.5, Fig. 3b), the rods become shorter and more uniform in size and shape. With increased substitution (x = 1, Fig. 3c), the morphology evolves further, forming uniformly thin particles with an overall reduction in size. This suggests that phosphorous incorporation reduces crystal particle size. This reduction in particle size is expected to shorten the lithium-ion diffusion paths for the phosphorous doped materials, thus enhancing the electrochemical rate performance.

The Raman spectra for the 3 compounds are shown in Fig. 4, and all show similar features, with characteristic bands for a Wadsley–Roth structure. In particular, the bands around 900 and 1000 cm^{-1} are characteristic of Wadsley–Roth phases, indicative of the presence of edge sharing octahedra. These

bands are not present in non-Wadsley–Roth T-Nb_2O_5 (tungsten bronze-like structure; Raman spectrum shown in Fig. S5), which do not possess edge sharing octahedra. All the peaks associated with the bond stretching modes (600–1000 cm^{-1}) show a shift to higher wavenumbers, indicating a strengthening of the bonds on increasing P incorporation (this shift can clearly be seen in the expanded view of the region around 900 cm^{-1} shown in Fig. 4b). These spectral shifts confirm that phosphorous incorporation significantly impacts the bonding environment, most likely related to the resultant increased W occupation of the octahedral sites.

Electrochemical performance

The charge–discharge voltage profiles for the samples during the first formation cycle (at a current density of 0.01 A g^{-1}) are presented in Fig. 5. Undoped NWO exhibits a characteristic sloping voltage at high and low voltages, indicative of solid-solution behaviour, with a plateau-like region at ~1.6–1.7 V, more representative of a two-phase like regime. On P-doping the voltage profiles shift to higher voltage, and the whole profile exhibits a more sloping behaviour, and thus solid solution range for the whole voltage range. Notably, the incorporation of phosphorous (x = 0.5 and x = 1) leads to higher overall capacities, specifically, x = 0.5 delivers a 1st cycle discharge capacity of 246(5) mAh g^{-1}, while x = 1 achieves around 251 (10) mAh g^{-1}, both of which are significantly higher than the 217(1) mAh g^{-1} capacity of the undoped NWO material. This may in part relate to the above small shift in the voltage profiles to higher voltage, which brings additional capacity into

Fig. 3 Scanning electron microscopy (SEM) image of (a) $Nb_{14}W_3O_{44}$, (b) $Nb_{13.5}P_{0.5}W_3O_{44}$ and (c) $Nb_{13}PW_3O_{44}$.
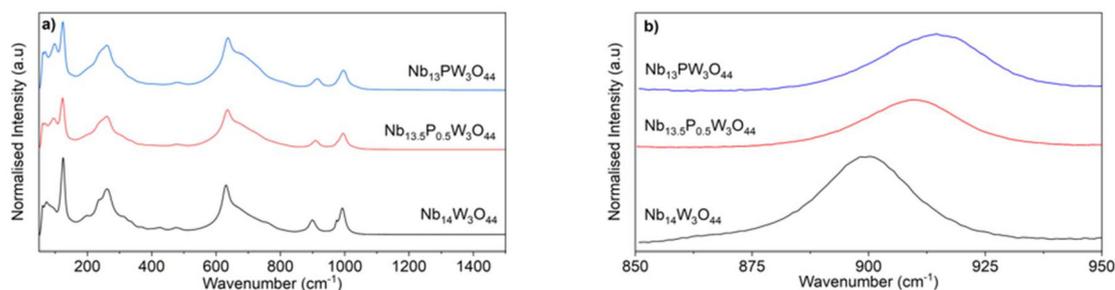
Fig. 4 Raman spectra of $Nb_{14}W_3O_{44}$ (black), $Nb_{13.5}P_{0.5}W_3O_{44}$ (red) and $Nb_{13}PW_3O_{44}$ (blue) (a). Raman spectra of $Nb_{14}W_3O_{44}$ (black), $Nb_{13.5}P_{0.5}W_3O_{44}$ (red) and $Nb_{13}PW_3O_{44}$ (blue) zoomed in view of the region around 900 cm^{-1} (b).
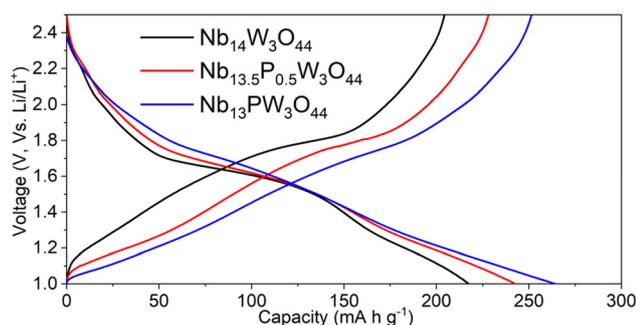
Fig. 5 Galvanostatic charge–discharge curves for the first cycle of $Nb_{14}W_3O_{44}$ (black), $Nb_{13.5}P_{0.5}W_3O_{44}$ (red) and $Nb_{13}PW_3O_{44}$ (blue), *vs.* lithium metal, with a current density of 0.01 A g^{-1} applied.

the voltage window (such extra capacity being below the 1 V cut-off for the undoped phase). In particular, it may relate to the replacement of W in the tetrahedral sites by P, which correspondingly leads to greater occupancy of the octahedral sites by the more reducible W. The results, thus, indicate that P-doping appears to increase the electrochemical capacity of the materials. Between the 1st and 3rd formation cycles, for all 3 materials, there is a clear drop in capacity, as observed for other Wadsley–Roth systems (Fig. S6). For undoped NWO the capacity drops to 206(9) mAh g^{-1}, corresponding to a 5% drop in capacity, x = 0.5 shows a drop to 231(3) mAh g^{-1}, corresponding to a similar 6% drop in capacity, while x = 1 shows a

much smaller (2%) drop to 244(11) mAh g^{-1}. These differences can also be seen in the dQ/dV profiles, where small differences are seen for the undoped and x = 0.5 sample between these cycles, while negligible change is seen for the x = 1 sample (Fig. S7). The dQ/dV curves also indicate an increase in capacitive contributions for the phosphorous doped phases, consistent with the smaller particle sizes and larger active surface area of the phosphorous doped samples. Overall the observed capacity decreases are significantly lower than observed for related (3 × 3) block structures, containing reducible metals in tetrahedral sites ($Nb_7Ti_{1.5}Mo_{1.5}O_{25}$ has a 15% capacity drop between the 1st and 2nd cycle),[30] nevertheless larger changes are seen at higher current densities (discussed below). Table S4 shows the difference in the number of intercalated lithium for the first and third cycles for all 3 materials. For NWO less lithium ions are intercalated into the material compared to the P-doped compositions, 22 lithium ions (NWO) compared to 23 lithium ions (x = 0.5 and x = 1).

To evaluate the electrochemical rate performance and capacity retention of the three compositions, additional measurements were conducted at varying current densities (0.1–4 A g^{-1}) under asymmetric cycling conditions (1.0–2.5 V window), where the lithiation rate was fixed at 0.1 A g^{-1}, and the delithiation rate was progressively increased (Fig. 6). While there were only small differences in the capacity drops on the initial formation cycles, larger differences were seen between the capacities at 0.01 A g^{-1} *versus* 0.1 A g^{-1}. In particular, the undoped phase exhibits a larger capacity drop from 0.01 A g^{-1}
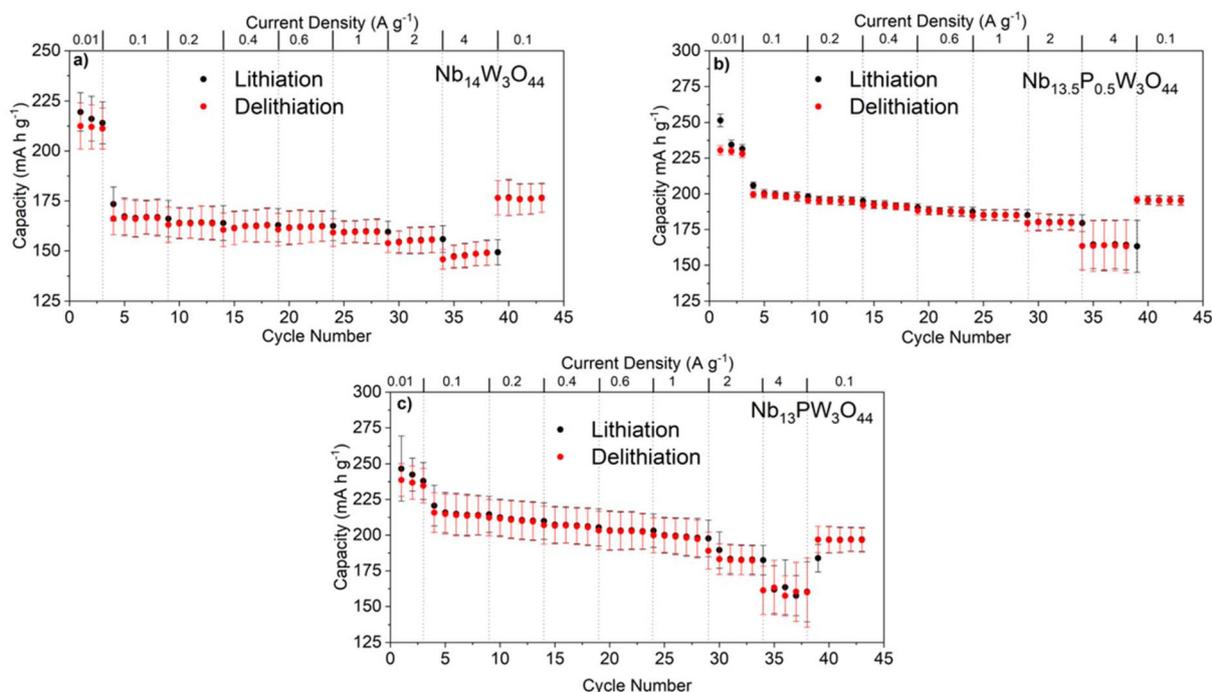

Fig. 6 Average specific capacities of (a) two $Nb_{14}W_3O_{44}$ cells, (b) two $Nb_{13.5}P_{0.5}W_3O_{44}$ cells and (c) two $Nb_{13}PW_3O_{44}$ cells undergoing asymmetric cycling – such that the lithiation current density is maintained at 0.1 A g^{-1}, while the delithiation gradually increases after 5 cycles at each rate step. The black error bars are for lithiation, the red ones are for the delithiation.
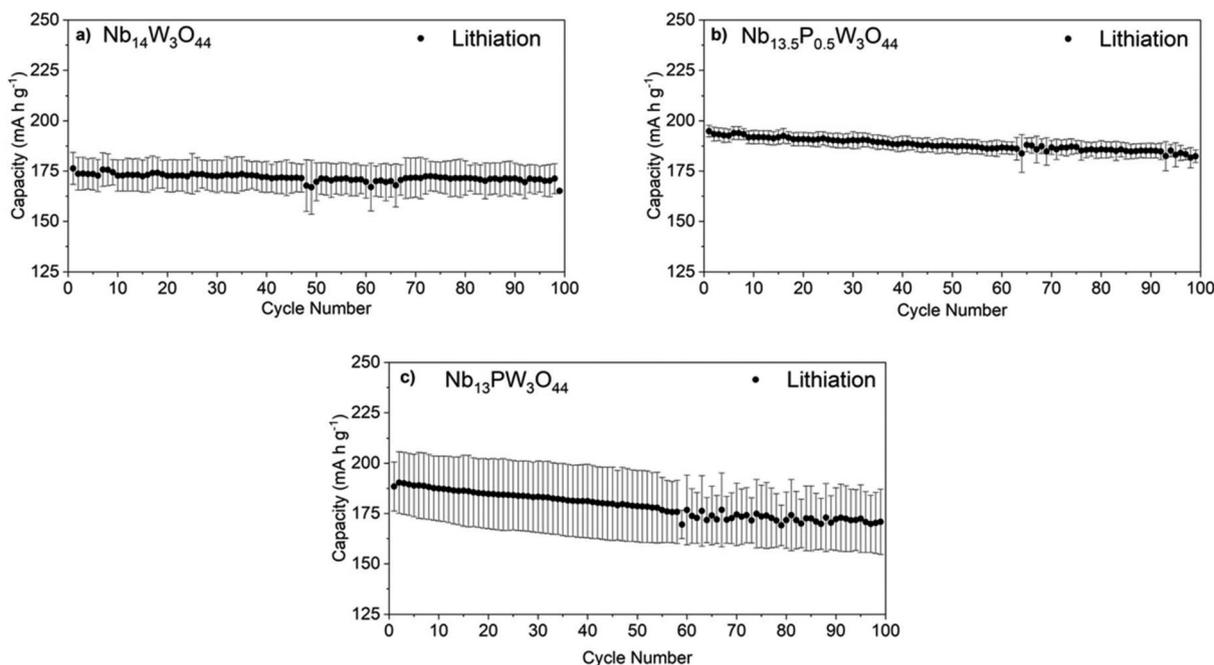
Fig. 7 Long term cycling data for duplicate cells. (a) $Nb_{14}W_3O_{44}$, (b) $Nb_{13.5}P_{0.5}W_3O_{44}$ and (c) $Nb_{13}PW_3O_{44}$. 100 cycles were performed symmetrically at a current density of 0.6 A g^{-1}.

to 0.1 A g^{-1} compared to the P-doped compositions, with decreases of 20%, 12%, and 7% for the NWO, x = 0.5, and x = 1 phases, respectively, indicating here the beneficial effect of replacing reducible W in the tetrahedral sites by non-reducible P. In particular, a drop in the capacity in the region 1.0–1.6 V is seen in both voltage profiles and dQ/dV plots, with this being particularly large for the undoped sample (Fig. S6 and S7).

For all samples, capacity retention remains strong at higher current densities, indicating excellent rate capability in all these compositions, with NWO, x = 0.5 and x = 1 retaining capacities of 148(5), 163(15), and 166(12) mAh g^{-1} at 4 A g^{-1} respectively. The excellent rate performance could be related to the smaller particle sizes observed for the phosphorous doped samples, which helps to facilitate lithium-ion intercalation/deintercalation due to smaller diffusion pathlengths. Interestingly, while the initial capacities were higher for the P-doped samples, the capacity recovery at 0.1 A g^{-1} after the rate tests was best for the undoped and x = 0.5 samples.

To evaluate the cycling performance further, longer-term cycling was conducted on all three materials, confirming good capacity retention over 100 cycles at a current density of 0.6 A g^{-1} (~3C) (Fig. 7). The data show that the undoped sample starts with an initial capacity of 176(8) mAh g^{-1}, which drops to 165(1) mAh g^{-1} after the 100th cycle giving a capacity retention of 93%. The x = 0.5 sample (Fig. 7b) shows improved performance, with an initial capacity of 194(3) mAh g^{-1}, which drops to 185(3) mAh g^{-1} after the 100th cycle giving a capacity retention of 95%. The highest phosphorous content sample, x = 1 (Fig. 7c), shows the highest capacity fade and largest variation in cells, with an initial capacity of 191(15) mAh g^{-1}, which drops to 171(16) mAh g^{-1} after the 100th cycle corres-

ponding to a capacity retention of 90%. This increased capacity fade may be linked to its smaller particle size, which increases the surface area of the particles increasing the extent of electrode–electrolyte interactions which facilitate parasitic side reactions that degrade capacity retention over time. Overall, the P-doped phases outperform the undoped material in terms of capacity, however, the x = 0.5 phase has the best capacity retention over 100 cycles at 0.6 A g^{-1}.

Conclusions

In conclusion, we have demonstrated for the first time the synthesis of P doped $Nb_{14}W_3O_{44}$, with Rietveld refinement confirming the successful incorporation of phosphorous. Electrochemical testing, within a lithium-half cell, revealed that P-doping significantly improved the initial capacity of the NWO material. Rate performance also improved, with the doped ($Nb_{14-x}P_xW_3O_{44}$) samples exhibiting higher capacities at increased current densities. At a high rate of 4 A g^{-1}, the x = 0.5 and x = 1 materials retained capacities of 163(15) and 166(12) mAh g^{-1} respectively, outperforming the undoped material, which retained just 148(5) mAh g^{-1} at 4 A g^{-1}. Long-term cycling at 0.6 A g^{-1} demonstrated excellent cycling stability and capacity retention, with the x = 0.5 performing best, maintaining 95% of its capacity after 100 cycles. While the x = 1 sample showed the highest initial capacity, it experienced greater capacity fade over time, suggesting further optimisation of this composition is required. Overall, the enhanced electrochemical performance observed in the P-doped compositions highlights the potential of site-selective doping strat-

egies for both structure and morphology control to improve the electrochemical properties in Wadsley–Roth niobate anodes with tetrahedral sites, suggesting further studies are warranted in this area.

Author contributions

Conflicts of interest

There are no conflicts to declare.

Data availability

Data sets available: **https://doi.org/10.25500/edata.bham.00001360**.

Supplementary information (SI) (structure refinement information, and electrochemistry plots) is available. See DOI: **https://doi.org/10.1039/d5dt02060c**.

Acknowledgements

References

1 L. K. K. Maia, L. Drünert, F. La Mantia and E. Zondervan, *J. Cleaner Prod.*, 2019, **225**, 928–938.

2 C. P. Grey and D. S. Hall, *Nat. Commun.*, 2020, **11**, 6279.

3 D. Deng, *Energy Sci. Eng.*, 2015, **3**, 385–418.

4 H. Zhang, Y. Yang, D. Ren, L. Wang and X. He, *Energy Storage Mater.*, 2021, **36**, 147–170.

5 X. Xu, S. Wang, H. Wang, C. Hu, Y. Jin, J. Liu and H. Yan, *J. Energy Chem.*, 2018, **27**, 513–527.

6 E. Ferg, R. J. Gummow, A. de Kock and M. M. Thackeray, *J. Electrochem. Soc.*, 1994, **141**, L147.

7 M. M. Thackeray and K. Amine, *Nat. Energy*, 2021, **6**, 683–683.

8 A. D. Robertson, L. Trevino, H. Tukamoto and J. T. S. Irvine, *J. Power Sources*, 1999, **81–82**, 352–357.

9 Y.-J. Hao, Q.-Y. Lai, J.-Z. Lu and X.-Y. Ji, *Ionics*, 2007, **13**, 369–373.

10 C. M. Julien and A. Mauger, *Micromachines*, 2024, **15**, 310.

11 X. Ding, Q. Zhou, X. Li and X. Xiong, *Chem. Commun.*, 2024, **60**, 2472–2488.

12 S. Andersson and A. D. Wadsley, *Nature*, 1966, **211**, 581–583.

13 R. J. Cava, D. W. Murphy and S. M. Zahurak, *J. Electrochem. Soc.*, 1983, **130**, 2345.

14 Y. Sheng, Y. Wang, S. Yin, L. Zhao, X. Zhang, D. Liu and G. Wen, *Chem. – Eur. J.*, 2024, **30**, e202302865.

15 C. P. Koçer, K. J. Griffith, C. P. Grey and A. J. Morris, *J. Am. Chem. Soc.*, 2019, **141**, 15121–15134.

16 S. Geng, Y. Zhang, L. Shi, A. Shi, L. Zhou, C. Kang, Z. Qiang, J. Zhu, S. Dong, D. Li, G. Yin and S. Lou, *Energy Storage Mater.*, 2024, **68**, 103339.

17 Toshiba researchers use TiNb2O7 anodes for high-energy, fast-charging, long-life Li-ion batteries for EVs, **https://www.greencarcongress.com/2018/07/20180706-toshiba.html**, (accessed 18 Septemebr 2024).

18 N. Takami, K. Ise, Y. Harada, T. Iwasaki, T. Kishi and K. Hoshina, *J. Power Sources*, 2018, **396**, 429–436.

19 K. J. Griffith, Y. Harada, S. Egusa, R. M. Ribas, R. S. Monteiro, R. B. Von Dreele, A. K. Cheetham, R. J. Cava, C. P. Grey and J. B. Goodenough, *Chem. Mater.*, 2023, **33**, 4–18.

20 A. J. Green, E. H. Driscoll, P. A. Anderson, E. Kendrick and P. R. Slater, *J. Mater. Chem. A*, 2024, **12**, 7321–7328.

21 C. Yang, S. Deng, C. Lin, S. Lin, Y. Chen, J. Li and H. Wu, *Nanoscale*, 2016, **8**, 18792–18799.

22 K. J. Griffith, Y. Harada, S. Egusa, R. M. Ribas, R. S. Monteiro, R. B. Von Dreele, A. K. Cheetham, R. J. Cava, C. P. Grey and J. B. Goodenough, *Chem. Mater.*, 2021, **33**, 4–18.

23 L. Yan, H. Lan, H. Yu, S. Qian, X. Cheng, N. Long, R. Zhang, M. Shui and J. Shu, *J. Mater. Chem. A*, 2017, **5**, 8972–8980.

24 L. Yan, X. Cheng, H. Yu, H. Zhu, T. Liu, R. Zheng, R. Zhang, M. Shui and J. Shu, *Energy Storage Mater.*, 2018, **14**, 159–168.

25 L. Yan, J. Shu, C. Li, X. Cheng, H. Zhu, H. Yu, C. Zhang, Y. Zheng, Y. Xie and Z. Guo, *Energy Storage Mater.*, 2019, **16**, 535–544.

26 X. Huang, W. Zhou, X. Chen, C. Jiang and Z. Zou, *Electrochim. Acta*, 2021, **368**, 137613.

27 R. S. Roth and A. D. Wadsley, *Acta. Crystallogr.*, 1965, **19**, 38–42.

28 J. G. Allpress and A. D. Wadsley, *J. Solid State Chem.*, 1969, **1**, 28–38.

29 O. A. Drozhzhin, V. V. Grigoryev, A. M. Alekseeva, R. R. Samigullin, D. A. Aksyonov, O. V. Boytsova, D. Chernyshov, V. V. Shapovalov, A. A. Guda, A. V. Soldatov, K. J. Stevenson, A. M. Abakumov and E. V. Antipov, *ACS Appl. Mater. Interfaces*, 2021, **13**, 56366–56374.

30 A. J. Green, E. H. Driscoll, Y. Lakhdar, E. Kendrick and P. R. Slater, *Dalton Trans.*, 2023, **52**, 13110–13118.

31 Y. Lakhdar, H. Geary, M. Houck, D. Gastol, A. S. Groombridge, P. R. Slater and E. Kendrick, *ACS Appl. Energy Mater.*, 2022, **5**, 11229–11240.

32 Y. Lakhdar, Y. Chen, H. Geary, M. E. Houck, A. S. Groombridge, P. R. Slater and E. Kendrick, *J. Power Sources*, 2023, **588**, 233710.

33 K. J. Griffith, K. M. Wiaderek, G. Cibin, L. E. Marbella and C. P. Grey, *Nature*, 2018, **559**, 556–563.

34 E. H. Driscoll, A. Green, D. Fortes, C. Howard, L. L. Driscoll, E. Kendrick, C. Greaves and P. R. Slater, *Chem. Commun.*, 2024, **60**, 10001–10004.

35 J. M. Sieffert, C. J. Lang, S. Bazylevych, S. Jia and E. McCalla, *J. Mater. Chem. A*, 2024, **12**, 1429–1437.

36 R. S. Roth and A. D. Wadsley, *Acta. Crystallogr.*, 1965, **19**, 26–32.

37 A. K. Cheetham and N. C. Allen, *J. Chem. Soc., Chem. Commun.*, 1983, 1370–1372.

38 K. Momma and F. Izumi, *J. Appl. Crystallogr.*, 2011, **44**, 1272–1276.

39 M. T. Casais, E. Gutiérrez-Puebla, M. A. Monge, I. Rasines and C. Ruíz-Valero, *J. Solid State Chem.*, 1993, **102**, 261–266.

40 S. Patoux, M. Dolle, G. Rousse and C. Masquelier, *J. Electrochem. Soc.*, 2002, **149**, A391.

41 C. Jiang, T. Liu, N. Long, X. Cheng, N. Peng, J. Zhang, R. Zheng, H. Yu and J. Shu, *Ceram. Int.*, 2019, **45**, 18111–18114.

42 B. H. Toby and R. B. Von Dreele, *J. Appl. Crystallogr.*, 2013, **46**, 544–549.